

RESEARCH ARTICLE

Impact of structural short-range order and tetrahedral germanium on electronic and dielectric properties in phase-change materials

M. Micoulaut¹  | H. Flores-Ruiz² 

¹Laboratoire de Physique Théorique de la Matière Condensée, Sorbonne Université, Paris Cedex 05, France

²Departamento de Ciencias Naturales y Exactas, CUValles, Universidad de Guadalajara, Ameca, Jalisco, Mexico

Correspondence

M. Micoulaut, Sorbonne Université, Laboratoire de Physique Théorique de la Matière Condensée, CNRS UMR 7600, 4 Place Jussieu, 75252 Paris Cedex 05, France.

Email: mmi@lptmc.jussieu.fr

Funding information

CONACYT 321139/ECOS-Nord, Grant/Award Number: M21P01

Abstract

The optoelectronic properties of prototypical Telluride amorphous phase-change materials (GeTe and Ge₂Sb₂Te₅) are investigated from ab initio molecular dynamics simulations. Local tetrahedral germanium geometries are identified from topological angular constraint counting and this permits to relate exactly their contribution to targeted properties. The analysis of our computation reveals that the dominant population of tetrahedral Ge contributes to the tail of the valence and conduction band but with an increased electronic localization for the latter, whereas residual (essentially octahedral) geometries induce an overall constant localization at $E > E_F$ except close to the Fermi gap, where p electrons are largely delocalized. The detailed calculation of the atomic dipoles in the amorphous state indicates that tetrahedral Ge leads to lower momenta, especially in a-GeTe, and corresponding Ge-based correlations with Wannier centers also indicate the dual nature of the local geometries. These features which drive optical and dielectric contrast exemplify the unique properties of phase-change materials, and represent an obvious breakdown of the well-known Zachariasen rule stating that the short-range order is similar in crystals and glasses.

KEYWORDS

glass, molecular dynamics, tellurium/tellurium compounds

1 | INTRODUCTION

Phase-change (PC) materials such as chalcogenide alloys present a rapid transition between an amorphous (a) semi-conducting state and a crystalline (c) conducting one which induces a remarkable contrast in optical and electrical properties.^{1,2} As such, these materials appear to be very attractive for optical recording or non-volatile data storage applications.³ They also represent benchmark systems of the basic nature because of their underlying topological phases,^{4,5} and their structural and bonding change during the a↔c transition that affects both electronic and dielectric properties.⁶ Chalcogenides do indeed exhibit a

profound modification in bonding from covalent to metallic that is obviously modified during the PC switching, and which also depends on thermodynamic conditions and composition. Among structural properties, the most spectacular feature is probably the important difference in short-range order (SRO) that represents an obvious breakdown of the well-known Zachariasen rule stating that crystals and glasses have the same SRO.⁷ With such a different SRO, one thus expects to see the structural motifs deeply involved in the PC phenomena with sp³ hybridized tetrahedra typical of covalent semiconductors, whereas p-bonded octahedra will facilitate conduction. This issue is obviously part of a more general topic that concentrates

on the linkage between structural features of disordered materials with their optoelectronic characteristics.⁸

Early studies⁹ using X-ray absorption experiments have indicated that the germanium SRO in Ge-based tellurides can be rather different, and changes from a dominant p-bonded octahedral coordinated site as, for example, in trigonal GeTe to a more elusive geometry in the amorphous phase that continues to be debated¹⁰ and which seems to be made of both tetrahedral (T-Ge hereafter) and defect octahedral four-fold Ge, albeit contradicted by recent Mössbauer spectroscopy¹¹ which indicates that Ge occupies only tetrahedral sites in a-Ge₂Sb₂Te₅ (GST225 hereafter). Such experiments and many others (see Ref. [1] for a review) certainly characterize in more detail the structure of the amorphous state but can hardly establish a direct correlation between the local atomic order and macroscopic measurements and/or crucial properties regarding the PC application. Theoretical investigations using atomic simulations are, therefore, welcome,^{12–16} and these have emphasized the central role played by squared-membered rings^{12,17} that have been independently confirmed¹⁸ from anomalous X-ray scattering (AXS), the latter also suggesting that Ge atoms dominate the formation of square rings with highly puckered shapes, and the coexistence of a near 50:50 mixture of T-Ge and R-Ge. We have hence examined from molecular simulations the electronic and dielectric properties of two prototypical PC materials, a-GeTe and a-GST225. Previous investigations in this direction¹⁹ have suggested that the large optical contrast between crystalline and amorphous PCMs arise from a large difference in the optical matrix elements which contribute to the dielectric function $\epsilon(\omega)$ (or optical conductivity). For GeTe, such elements have been found to be enhanced in the crystalline phase because of aligned rows of resonantly bonded p orbitals, in contrast with amorphous phases where disorder basically cancels out such effect, together with a loss in medium-range ordering.^{20,21} As a result, both $\epsilon(0)$ and ϵ_∞ are found to be substantially different²² in the crystal and the amorphous phase and lead to a permittivity contrast.

Here, we adopt a slightly different approach by focusing on the effect of PCM base geometries since it is known that SRO together with charge localization/delocalization is known to contribute locally to polarization, the obvious symmetric tetrahedral geometry leading to an obvious nonpolar character. By identifying the typical SRO elements/geometries of such materials, we elucidate the correlation between SRO characteristics and base geometries with electronic and dielectric features of PC materials. The profound differences which emerge from both populations (T- and residual Ge) suggest that in PC materials SRO alteration prevails between the crystalline and the amorphous state, unlike conventional “Zachariasen” glasses,

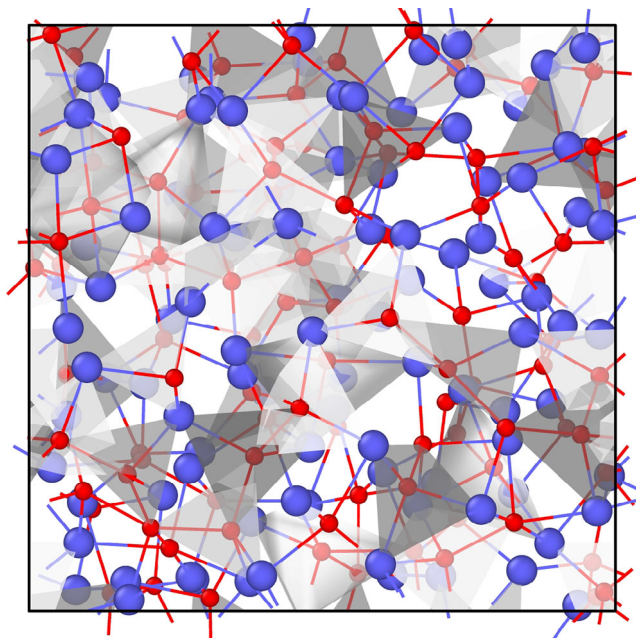


FIGURE 1 The simulation box of the amorphous GeTe 200 atom model. Ge tetrahedra (T-Ge) are indicated in grey, according to a topological constraint count (see below). Te atoms are in blue.

and is responsible for subtle properties close to the Fermi level. The use of maximally localized Wannier functions (MLWF) to determine local dipolar momenta permits to gain quantitative information on the contribution of distinct geometries to the total dipole moment or to the polarization. This has not been fully explored so far.

2 | SIMULATION DETAILS

Results are based on structure models (Figure 1) of amorphous PC materials that have been generated from ab initio molecular dynamics (MD) using density functional theory (DFT-D2^{23,24}).

For amorphous GeTe,²⁵ they consist in three independently quenched 200 atom configurations that have been equilibrated in the liquid state at 820 K prior to a quench to 300 K and statistical averages over 40 ps. MD simulations of Car-Parrinello type (CPMD code) were performed in a cubic box of size L with periodic boundary conditions and a density equal to experimental²⁶ ones ($N/L^3=0.0337 \text{ \AA}^{-3}$). The electronic structure has been described within DFT with an exchange-correlation energy obtained by Perdew, Burke, and Ernzerhof²⁷ (termed PBEsol), and evolved self-consistently during the motion. A generalized gradient approximation (GGA) has been used, and valence electrons were treated explicitly, in conjunction with Troullier–Martins norm-conserving pseudopotentials. The wavefunctions were expanded at

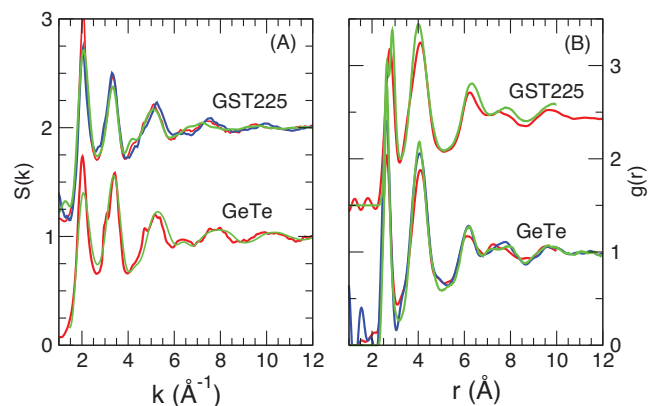


FIGURE 2 Calculated (green) structure factor $S(k)$ (A) and pair correlation function $g(r)$ (B) of GST225 and GeTe models, compared to experimental data from X-ray scattering in reciprocal (red²⁶ and blue curves,³⁴ panel a) and real space (red²⁶ and blue curves,³⁰ panel b).

the Γ point of the supercell on a plane-wave basis set with an energy cutoff of 20 Ry. During the CPMD simulation, a fictitious electron mass of 2000 a.u. and a timestep of 0.12–0.36 fs was used to integrate the equations of motion. The equilibrated trajectories of similar compositions have led to an excellent agreement of measured structure functions from neutron and X-ray scattering in the liquid and amorphous state^{25,28,29} (Figure 2).

The same strategy has been employed for GST225,⁵ and the resulting structure at 300 K used for the present purpose was obtained from four independent quenches, starting from equilibrated configurations analyzed previously in the liquid state, and, again, successfully compared to experiments.³¹ All were obtained by quenching (≈ 10 K/ps) independent configurations of the equilibrated liquids obtained at 820 K. For all four configurations, the subsequent quenching was as follows: a 600 K plateau for 20 ps followed by a relaxation at 300 K for 50 ps. The electronic scheme was identical to the one used for GeTe. We refer the reader to Ref. [5, 31] more details.

The obtained structure GeTe and GST225 models have been analyzed in detail.^{5,25} We provide here a survey in order to be self-consistent. The calculated structure factor $S(k)$ and $g(r)$ reproduce very accurately the corresponding measured functions from X-ray scattering (Figure 1). Central to this agreement is the incorporation of dispersion forces^{23,24} (DFT-D2 scheme) that reduce the calculated Ge–Te bond distance which is overestimated (2.70 Å) in regular DFT simulations, and brings it closer (2.66 Å) to experimental measurements³² (2.62 Å). The comparison of numerical studies with partial correlations from AXS has been performed on a-GeTe²⁵ and GST225.⁵ The analysis of the former reveals that both Ge and Te partial

AXS patterns (peak positions, widths, and amplitudes) are rather well from simulation reproduced with a small contribution of the Ge partial to the principal peak at about $k \approx 2.0 \text{ \AA}^{-1}$ (Figure 1A), in contrast with regular DFT simulations which not only fail to reproduce typical peaks at $\approx 6 \text{ \AA}^{-1}$ but also induce a spurious phase lag in the experimental X-ray absorption (EXAFS) spectra.³²

Partial correlations in GST225 lead to a similar agreement with Ge and Te-based AXS partials,^{18,33} although a slight shift of the principal peak in the Sb partials being obtained. The comparison with reverse Monte Carlo simulations^{18,33–35} in real space shows that all structure models are consistent as all partial correlation functions are similar in terms of first and second-shell correlations, except for the presence of Te–Te homopolar defects which are barely present in DFT-D2.

The central findings of these DFT-D2 studies have been the presence of important topological disorder that consists in miscoordinations and mixed geometries, among which tetrahedral Ge sites which represent the dominant motifs (55% for GST225), consistently with Mössbauer spectroscopy measurements¹¹ and AXS.¹⁸ Sb sites change from a dominant pyramidal geometry typical of Group V chalcogenides to a defect octahedral one which is reminiscent³⁶ of the PC crystalline polymorph Sb_2Te_3 . A similar situation holds for a-GeTe which contains about 65% Ge tetrahedra²⁵ in the considered structure models (Figure 2). For the purpose of comparison, we have also studied a 300 atom c-GeTe in a trigonal geometry (space group R_{3m})³⁷ that can be viewed as a distorted rocksalt cell. After 10 ps relaxation at 300 K, it leads to the presence of a slightly distorted octahedral geometry⁹ for the Ge atoms which display three short and three long bonds, and corresponding bond lengths were found to be 2.81 and 3.20 Å (experimentally 2.82–2.84 Å and 3.17–3.18 Å, respectively³⁷).

It should be mentioned that hybrid functionals might lead to more accurate results, and especially to a better defined band gap. Unfortunately, the use of such functionals for the considered system sizes induces computational costs that are too high to be of practical use.

3 | ELECTRONIC PROPERTIES

3.1 | Band and orbital detail

From the different amorphous structure and c-GeTe models, we have performed from the Kohn–Sham (KS) eigenstates the calculation of the electronic density of states (EDOS) which are displayed in Figure 3B. X-ray photoemission spectroscopy (XPS) studies³⁸ have emphasized the important difference in density of states of amorphous

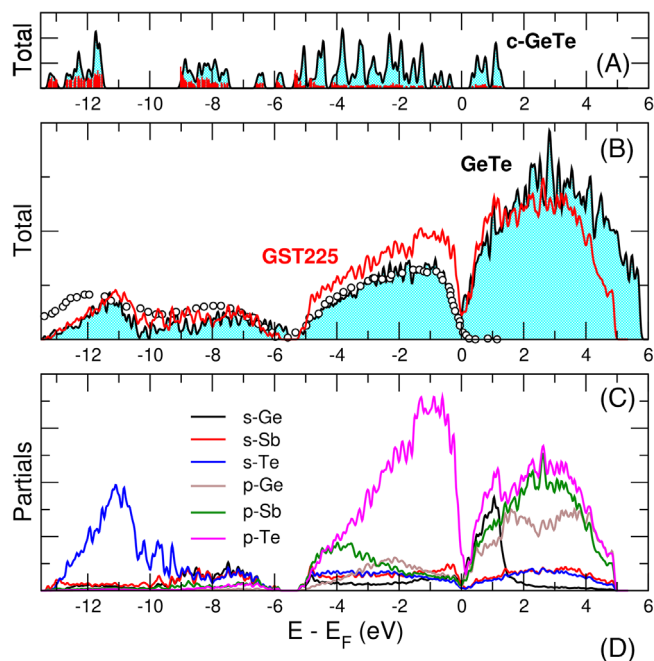


FIGURE 3 (A) Calculated total electronic density of states (EDOS) of trigonal GeTe (R_{3m}) together with the inverse participation ratio (IPR, red bars). (B) EDOS of a-GST225 (red) and a-GeTe (black). Experimental data (circles) are from Ref. [39]. (C) Decomposition into partial (s) and (p) contributions for a-GST225.

and crystalline GeTe (Figure 3A). We first note that for GeTe, the calculated valence band structure reproduces rather well experimental results obtained from XPS.³⁹ The obtained profile can be understood in terms of a contribution of s-orbitals of Ge and Te centered at -8.0 and -11.5 eV, respectively, together with a broad band close to the Fermi level that is dominated by p-orbitals of Te atoms in both GeTe and GST225 (Figure 3C). The projected EDOS furthermore shows that the low energy bands relate to s-contributions from Te, centered at -11.6 eV (Figure 3C), the conduction band being dominated by contributions from p-orbitals of all species (Ge, Sb, and Te in GST225) but also from s-Ge orbitals. Similar features are obtained for GeTe.⁴⁰

3.2 | Contribution from tetrahedral Ge

We use a topological constraint analysis^{10,25} to identify without any ambiguity tetrahedral geometries from angular excursions, instead of considering either bond lengths⁴¹ or angles between two well-defined geometries which lead to an obvious overlap in a global bond angle distribution (tetrahedral 109° and defect octahedral 90° – 100°). Here, we focus on angular excursions that are computed on-the-fly from the MD trajectories. A set of $N(N-1)/2$ angles is considered from the N first neighbors around a central

Ge. The motion of this triplet leads to a partial bond angle distribution out of which a mean $\bar{\theta}$ and a standard deviation σ_θ can be computed for each Ge of the network. If six low standard (i.e., rigid) deviations σ_θ around a Ge atom are detected, a tetrahedron is identified because this geometry is defined by six rigid angles that give rise to corresponding low angular standard deviations.⁴² On system average, such typical “tetrahedral” angles are well defined, and lead to a corresponding angle that is, in fact, very close to the tetrahedral angle as analyzed in detail for GeTe²⁵ and different GST alloys.⁴⁰

The validity of the method has been checked on a variety of systems including the archetypal Ge–S and Ge–Se chalcogenides. Here, the topological constraint count from MD trajectories^{43,44} was able to reproduce exactly the Maxwell mean-field constraint count,⁴² providing confidence that it can be extended to the description of the topology of more complex amorphous systems such as the present one. In order to add some more tests, we have also investigated the c-GeTe system found in a distorted rock-salt geometry. It 300 K, results lead to 15 rigid angles for both Ge and Te atoms with $\sigma \simeq 10^\circ$ – 12° which is indicative of an octahedral arrangement as all angles defined by $N = 6$ neighbors display a small angular excursion. The topological nature of c-GeTe and a-GeTe is, thus, very different.

In the amorphous phase, the resulting T-Ge-centered bond angle distribution is found to be rather similar to archetypal tetrahedral network glasses¹⁰ with a substantial homopolar Ge–Ge bond statistics however, consistently with previous investigations.¹⁵ It should be furthermore stressed that the identification key builds on angular topological constraints which measure from the MD trajectories not angles but small angular excursions. We remind that a criterion based solely on angles is misleading because of the overlap of two angular distributions centered at rather close values: 109° for T-Ge and 90° – 98° for octahedral Ge. Once five of such small angular excursions (i.e., independent rigid constraints) are detected around a given Ge atom, one identifies a T-Ge which has a constraint density of $n_c = r_{Ge}/2+5 = 7$ if Ge is four-fold coordinated.¹⁰ Corresponding species-dependent projected wavefunctions $\Psi_{Ge}(\mathbf{r})$ are then sorted according to the geometrical motif: (i) T-Ge with fractions given above for a-GeTe¹⁰ and GST225⁵ and (ii) a residue (R-Ge) which consists of four-fold Ge in defect octahedral geometries ($r_{Ge} = 4$) but also miscoordinated species ($r_{Ge} = 3$ or 5). These represent minority Ge sites with statistics given by 8.0%, 14.0%, and 13.0% for three-, four- and five-fold R-Ge in a-GeTe. In GST225, the same statistics is 10.1%, 23.7%, and 10.1%. The detailed contribution of such R-Ge is displayed in Figure 4 for GeTe (panel a) and GST225 (panel b). Such additional analysis permits to

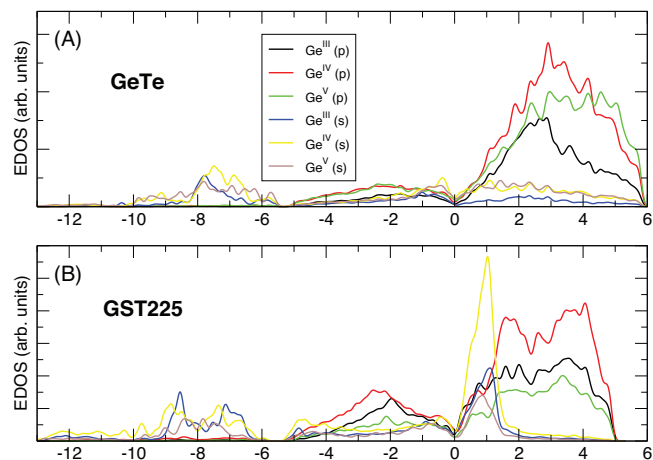


FIGURE 4 Decomposition into tetrahedral (T) and residual (R) contributions of the Germanium s and p-bands in GST225. The inset represents a focus around the Fermi level with the calculated EDOS of c-GeTe as reference (blue curve).

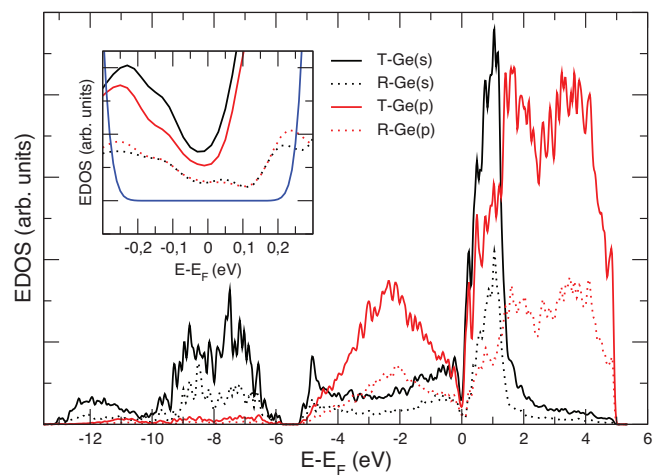


FIGURE 5 Contribution of r -fold ($r = \text{III, IV, V}$) residual germanium (R-Ge) to the s and p bands in the electronic density of states of amorphous GeTe (A) and GST225 (B).

detect that the contribution of the different r -coordinated species to the conduction band is not the same in both compounds. In GeTe, the high energy part is dominated by Ge^{IV} and Ge^{V} species, whereas all species contribute in GST225. In addition, the s-orbitals are found to dominate the conduction edge of the Fermi gap only in GST225 with a dominant contribution arising from four-fold Ge in the non-tetrahedral geometry. These features obviously establish a direct link between miscoordinations, geometries, and electronic contributions as also stressed for other amorphous systems.

Our first central finding is that T-Ge crucially influences the gap region, as revealed by Figure 5. Above the Fermi level, all orbitals contribute to the conduc-

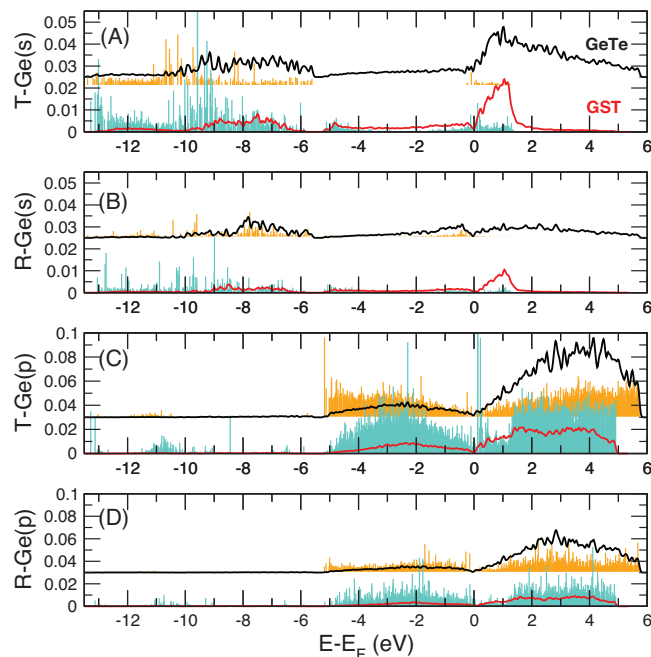


FIGURE 6 Calculated partial electronic contribution to s (A,B) and p bands (C,D) in a-GeTe (black) and GST225 (red, same as Figure 5) arising from tetrahedral (A and C) and residual (B and D) Ge atoms, together with the corresponding inverse participation ratios. Note that each band (S and P) has been put on the same scale (EDOS and IPR).

tion band for both GST225 (Figure 3C) and GeTe (see Figure 6), although a dominant Ge(s) orbital is acknowledged close to the Fermi gap at $E > E_F$. However, T-Ge atomic orbitals display a substantially increased contribution in both materials (Figure 5), and which leads for the T-Ge(s) orbital to a significant and sharp peak close to the conduction tail ($E - E_F \simeq 1.0$ eV, Figure 5), compatible with a conclusion drawn from a geometrical deconvolution of X-ray absorption spectra.⁴⁵ The decomposition into T-Ge and R-Ge furthermore indicates that the former is also responsible for the valence band edge that is dominated by both T-Ge(s) and T-Ge(p) orbitals.

Finally, the inspection of a blowup of the gap region (inset of Figure 5) permits to verify (i) the presence of increased midgap states for T-Ge with respect to R-Ge and (ii) the presence of an exponential Urbach tail⁴⁶ that is only detected for T-Ge contributions, and manifests by a rapid increase in the conduction band, similarly to amorphous Silicon⁴⁷ which is 100% tetrahedral. For GST225, a fit to the conduction band using $\exp[(E - E_F)/E_U]$ leads to an Urbach energy of $E_U = 68$ meV and 58 meV for T-Ge(p) and T-Ge(s), respectively. These values are similar to those found for a-GeTe (131 and 77 meV) but slightly smaller than those of amorphous silicon (200 meV⁴⁷).

3.3 | Localization properties

In character, T-Ge appear to display an increased electronic localization as shown in Figure 6 which represents both for a-GeTe and a-GST225 calculated Ge geometry-dependent EDOS (T-Ge or R-Ge) and the corresponding inverse participation ratios (IPR)

$$\text{IPR} = \int d\mathbf{r} |\Psi(\mathbf{r})|^4 \times \left(\int d\mathbf{r} |\Psi(\mathbf{r})|^2 \right)^{-2}. \quad (1)$$

The latter permits to measure the degree of localized orbitals as large value are usually indicative of localization around specific bonds, that is, $\text{IPR} \rightarrow 0$ for a fully delocalized state (conductor) and $\text{IPR} \rightarrow 1$ for a pure state. A combined inspection of GeTe and GST225 suggests an overall more localized bonding for the identified T-Ge as the signature of an increased covalent character (Figure 6A,C). It manifests by larger IPR values close to the edges of the conduction band (Figure 6A), the localization of residual Ge being substantially small in the region of the mobility edge corresponding to $E - E_F \simeq 0-1$ eV (Figure 6D).

One, furthermore, notes an increased localization for the s-band in the region $-13 \text{ eV} \leq E - E_F \leq -6 \text{ eV}$ (Figure 6A). Such a result mimics what has been recently observed in Se-enriched amorphous GeTe.⁴⁰ Here, the progressive transformation from GeTe into a tetrahedral GeSe network induces indeed, a more pronounced localization of the bonding for the latter which is consistent with its increased covalent character. It manifests by larger IPR close to the edges of the s-band, and hence s-Se bands. From our calculations, this effect is more pronounced in GST225 compared to GeTe, and suggest that the T-Ge bonding involved in the former is more localized/covalent. The residual Ge (R-Ge) does not exhibit any specific signature regarding localization as IPRs do not differ between Ge^{III} , Ge^{IV} , and Ge^{V} in both compounds (not shown).

3.4 | Dielectric properties from Wannier centers

We now establish relationship between T-Ge and a lower dipolar momentum (or polarizability). In order to relate dielectrics to atomic properties and bonding localization properties, we use the formalism of the boys localized orbitals.^{48,49} In a supercell approach, the boys localized orbitals are calculated as their periodic system generalization, corresponding to MLWF $w_n(\mathbf{r})$

$$w_n(\mathbf{r}) = \sum_{m=1}^J U_{mn} |\Phi_m\rangle \quad (2)$$

which provide an efficient way⁵⁰⁻⁵² to represent the electronic distribution around atoms in various materials⁵³⁻⁵⁵ from the J KS states Φ_m , the unitary matrix U_{nm} associated with the Bloch orbitals being determined by an iterative minimization of the Wannier function spread Ω in real space:

$$\Omega = -\frac{1}{(2\pi)^2} c_\alpha \ln |\langle \Phi_m | e^{i\mathbf{G}\cdot\mathbf{r}} | \Phi_m \rangle|^2 \quad (3)$$

where c_α are weights assigned to each x, y, z axes, and $G_\alpha = 2\pi/L$. The corresponding MLWF centers can then computed:

$$\bar{\mathbf{r}}_n^w = -\frac{L}{2\pi} \text{Im} \left[\ln \langle w_n | e^{i\mathbf{G}\cdot\mathbf{r}} | w_n \rangle \right]. \quad (4)$$

Next, we build on the atomic-based polarization theory⁵⁶ which establishes a link^{57,58} between MLWF centers and calculated dipole moments of ions in molecules or molecular networks. Such methods are used, for example, to determine, dispersive interactions of materials^{59,60} including tellurides.⁶¹ The partial dipole moment μ^i of a given atom i can be defined from the ion and the positions $\bar{\mathbf{r}}_n^w$ of the MLWF centers by assuming that the electronic charge is concentrated in point charges located on such centers:

$$\mu^i = \mu_I^i + \mu_e^i = Z_i \mathbf{R}_i - 2 \sum_{n \in i} \bar{\mathbf{r}}_n^w, \quad (5)$$

where Z_i and \mathbf{R}_i are the ionic charge and position of ion i , and the sum over $n \in i$ includes all the MLWF whose center is localized in the vicinity of $\mathbf{R}_i < r_m$.

Figure 7 now represents the calculated $\mu^i = |\mu^i|$ for both Ge and Te in amorphous GeTe and GST225. One acknowledges two main features. First, Te-related dipolar momenta are smaller than those of Ge which is related to the fact that charge separation between MLWF centers are smaller for the former. We, furthermore, note that Ge-based distributions display a broad range of values up to $\simeq 10^{-29}$ C m, the distribution being eventually bimodal for the case of GST225. With the identified T-Ge and R-Ge populations, we then represent the dipolar momenta (Figure 8) as a function of the total number of topological constraints n_c where $n_c = 7$ corresponds to the tetrahedral geometry since four-fold Ge leads to two radial constraints and 5 angles are needed to define a tetrahedra.²⁵

Differences between Te- and Ge-based results now appear in an increased fashion. The former displays a wide distribution of dipolar momenta (Figure 8B) and for both models μ does not seem to be correlated with the coordination number of Te atoms which are essentially two-fold ($n_c = 2$) or three-fold coordinated ($n_c = 4.5$). The

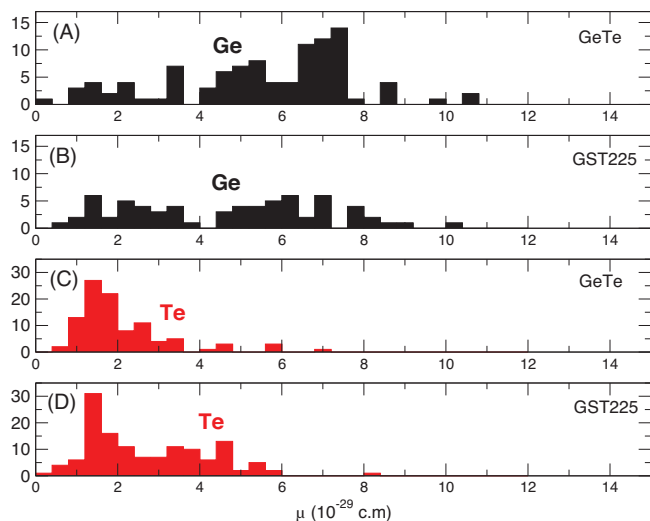


FIGURE 7 Dipolar moment distribution of Ge (black) and Te (red) in amorphous GeTe (A, C) and GST225 (B, D).

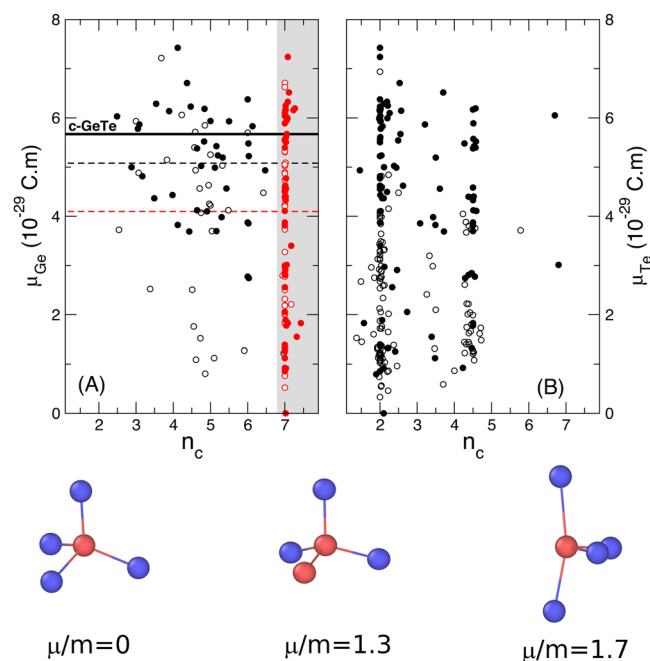


FIGURE 8 Dipolar moment distribution of Ge (A) and Te (B) in GeTe (filled circles) and GST225 (open circles) as a function of the total number of topological constraints n_c . Contributions from T-Ge are represented by red circles. The gray area corresponds to the tetrahedral zone with $n_c \approx 7$. Average μ for c-GeTe is indicated. Broken lines in panel (A) correspond to the average μ for T-Ge and R-Ge. Below panels a and b: typical SRO in PC materials with corresponding μ/m values.

situation appears to be radically different for the Ge atoms (Figure 8A). Here, small dipolar momenta are found for identified T-Ge atoms (i.e., $n_c = 7$), the correlation being particularly verified for a-GeTe. The correlation between low μ values and tetrahedral geometry appears,

indeed, increased for the latter and the reason might be that binary GeTe features less disorder than a ternary alloy such as GST225. Figure 8A obviously recalls the result of a perfect tetrahedron with identical bonds, which leads to $\mu_T \approx 0$ based on symmetry arguments. Any bond length fluctuation or symmetry breakdown induces $\mu_T \neq 0$ and for, for example, a T-Ge with n homopolar Ge-Ge bonds, one has $\mu_T = m[1 + (3 - n)\cos\theta_T]$ with m being the bond dipole moment and θ_T the tetrahedral angle (molecules in Figure 8). For SRO with an increased asymmetry such as defect octahedral Ge (embedded in the R-population) with two long bonds and two short bonds in the equatorial plane, the minimum estimate leads to $\mu_R = m\sqrt{2}$, any additional symmetry breaking leading to corresponding dipole moments that are even more increased. The average dipolar momentum for the T-Ge (broken red line, Figure 8A) appears, indeed, to be lower than the one of R-Ge and c-GeTe. The difference in SRO between c- and a-PCMs, thus, affects atomic dipolar moments, and ultimately impacts dielectric contrast that crucially depend on the fraction of tetrahedra.

4 | DISCUSSION

4.1 | Implications for structural correlations

There are obvious implications in terms of bonding and bonding distances. We have noticed previously that the T-Ge is responsible for the valence band edge that is dominated by both T-Ge(s) and T-Ge(p) orbitals (Figure 5). The valence tail is usually associated with short bonds⁴⁷ given here by a bond length of $d_{\text{Ge-Te}} = 2.53 \text{ \AA}$ on average for T-Ge (2.64 \AA on average for R-Ge) in a-GeTe. Corresponding calculated Ge-centered pair correlation functions (pdf) are displayed in Figure 9, where the pdf is a linear combination of both g_{GeGe} and g_{GeTe} . We also represent neighbor distribution functions (NDF) which correspond to distributions $\text{NDF}_i(r)$ where neighbors of rank i around a Ge atoms are sorted according to their distance. Such distributions have been helpful in decoding the distribution of short and long bonds in PCMs.^{41,62} The identification of tetrahedral geometries from constraints now leads to an unambiguous result regarding bond length properties in relationship with identified Ge geometries. It indicates, indeed, that $g_{\text{T-Ge}}(r)$ (panel a) displays well separated first and second shell of neighbors typical of lighter chalcogenides (Ge-S or Ge-Se^{44,63}), whereas this is not the case for the residual Ge atoms which (i) do not lead to the property $g(r_m) \rightarrow 0$ at the minimum r_m of the pdf, (ii) display bimodal distributions for the very first NDFs (colored curves, Figure 9B) which eventually extend⁴¹ to $r > r_m$, this being indicative of the

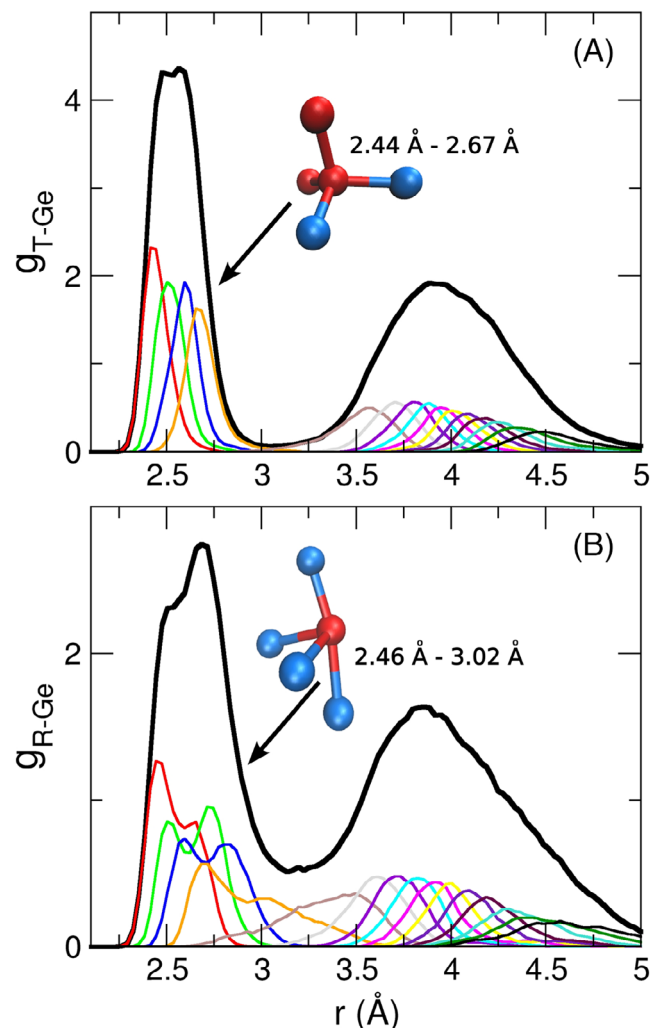


FIGURE 9 Calculated Ge-centered T-Ge (A) and R-Ge (B) pair correlation (thick black) and neighbor distribution functions $NDF_i(r)$ up to neighbor $i = 10$ (colored) in a-GeTe. Typical distances involved with the two geometries are indicated.

presence of both mixed geometries (pyramidal, defect octahedral) and coordinations ($r_{\text{Ge}} = 4-5$) that also obviously lead to the presence of short and long bonds as a signature of defect octahedral SRO.

4.2 | Correlations of Wannier centers

An inspection of the location of the MLWF centers (Figure 10) now also indicates the presence of obvious correlations between electronic charge location and the SRO Ge geometry. In GST225, defective octahedral sites (Sb or R-Ge) involve a s-type MLWF which corresponds to a lone pair (also detected on Te atoms), whereas other MLWFs are found along the short Ge–Te or Sb–Te bonds and correspond to localized p-type centers as also revealed from the larger participation ratios found close to the Fermi level

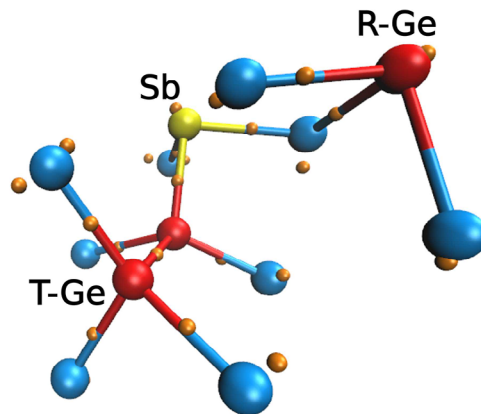


FIGURE 10 A fragment of the GST225 network with typical geometries: defect octahedral Sb (yellow), T-Ge and R-Ge (red), and Te (blue). Wannier centers are represented in orange.

(Figure 6D). Similarly, T-Ge exhibits four sp^3 -like MLWFs along the four Ge–Te or Ge–Ge bonds, while Te atoms displays either two or three p-type bonds, together with s-type lone pairs. Similar features are recognized on atomic snapshots of the present a-GeTe model (not shown) or discussed in nitrogen modified PCMs.⁶⁴

In Figure 11A are displayed the species (Ge, Sb, Te)-dependent correlation function with MLWF centers $g_{\text{Ge}W}(r)$ ($p = \text{Ge, Sb, Te}$). For both Te and Sb, one acknowledges a dominant peak at 0.3–0.4 Å which corresponds to the obvious presence of the non-bonding (lone pair) electrons, as also detected from the Wannier analysis of trigonal GeTe which displays a MLWF peak in $g_{\text{Te}W}$ at 0.3–0.4 Å. Such a peak is also detected in R-Ge at since lone pair electrons are also present for Ge atoms having a coordination different from 4. Conversely, $g_{\text{Ge}W}(r)$ exhibits for both GST225 (solid black curve) and GeTe (broken curve) distinct peaks at particular distances $0.25 \text{ \AA} \leq r \leq 1.60 \text{ \AA}$ that can be analyzed according to the established T-Ge and R-Ge populations (Figure 9B). For both populations R-Ge and T-Ge, a main peak is located in the vicinity of $\approx 1.35 \text{ \AA}$ which is a distance somewhat larger than half the typical Ge–Te bond length (Figure 11B). This value can be rationalized by invoking the larger electronegativity of Te atoms and the resulting electron charge transfer occurring toward the Te atoms upon formation of the Ge-centered geometries. Note that these features are clearly visible from the atomic snapshots (Figure 10) as MLWF centers along Ge–Te or Sb–Te bonds are shifted in the direction of the Te atoms.

The second feature visible in Figure 11B is the presence at very short distances (smaller than 0.5 Å) of an MLWF center that is only obtained for R-Ge atoms (red curves), specific to this geometry and is, once again, detected in trigonal GeTe at a somewhat smaller distance

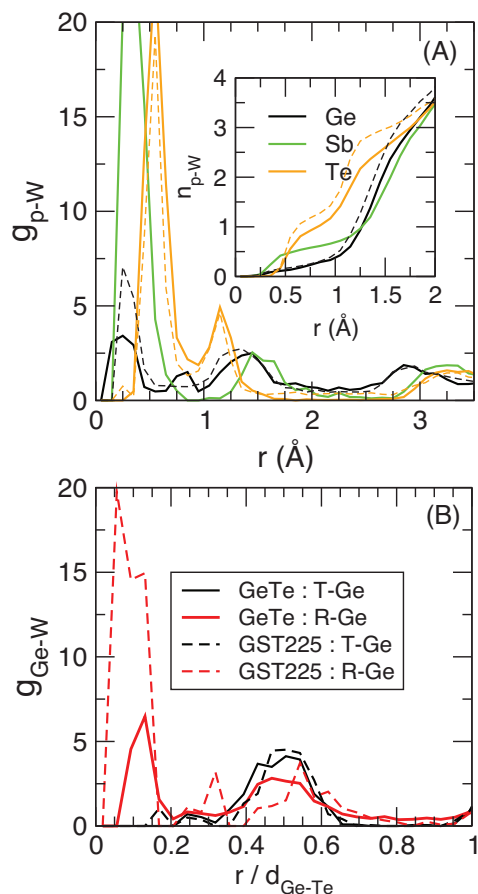


FIGURE 11 (A) Species-MLWF center pair correlation functions $g_{pW}(r)$ ($p = \text{Ge, Sb, Te}$) in a-GST225 and GeTe (broken lines). The inset represents the corresponding coordination number $n_{pW}(r)$. (B) Ge-MLWF center correlations g_{GeW} in a-GeTe (solid curves) and a-GST225 (broken curves) for identified T-(black) and R-Ge atoms (red) as a function of reduced distance $r/d_{\text{Ge-Te}}$ with $d_{\text{Ge-Te}} = 2.67 \text{ \AA}$.

(0.1–0.2 Å). This peak is due to nonbonding electrons lying close to the atoms being involved in defect octahedral or miscoordinated germanium.

Such correlations also permit to access to the fraction of R-Ge atoms since the s-type MLWF found at short distances ($r \leq 0.94 \text{ \AA}$) is specific of these non-tetrahedral geometries. The corresponding coordination number:

$$n_{\text{GeW}}(r) = 4\pi\rho_0 \int_0^r g_{\text{GeW}}(r_1)r_1^2 dr_1 \quad (6)$$

permits, indeed, to get the number of Ge with s-type lone pairs (inset of Figure 11A) at the minimum of the function g_{GeW} . Here, ρ_0 represents the system density. We obtain a fraction of R-Ge of 33% and 31% for GST225 and GeTe, respectively. These values are very close to those determined from topological constraints (45%⁵ and 33%²⁵) and,

highlight, once again that such materials are found in predominantly tetrahedral configuration.¹¹

4.3 | General comments regarding the phase-change mechanism

Previous investigations on the atomistic origin of dielectric contrast in PCMS¹⁹ have suggested that the dielectric contrast might arise from a loss in resonant bonding during the crystalline to amorphous transition, the loss being driven by the breakdown of ordering and alignment of p orbitals, irrespective of the coordination changes. The present results provide some additional insight into atomic scale aspects of the contrast. While it is, indeed, confirmed that the coordination number does not have an important impact on the PC phenomenon, the nature of the underlying dominant geometry in the amorphous phase (T-Ge) that can hardly lead to short-range alignment reduces substantially the possibility of having resonant bonding. This is reflected from the important contrast of the dipolar momentum. While the octahedral or distorted octahedral crystalline structure displays a rather large value ($6 \times 10^{-29} \text{ C m}$, Figure 8A), quenched amorphous phases lead, indeed, to Ge sites that are predominantly 4-coordinated with tetrahedral bond angles, and these lead to a lowering of the polarization in a-GeTe (Figure 8A). Such dominant tetrahedral features are unambiguously confirmed from the topological constraint count and from the Wannier function analysis of MLWF-Ge correlations. For GST225, the presence of additional species such as the predominantly pyramidal/defect octahedral Sb atoms induces a somewhat less marked picture as certain R-Ge atoms appear to have a low dipolar momentum as well. However, both compounds lead to enhanced localized electronic contributions for the s-bands close to the Fermi level, in both the valence and conduction bands (Figure 5), once the R-Ge populations are appropriately identified.¹⁰

PCM phenomena build on the electrical contrast between the crystalline and the amorphous phase. It is well known that the crystalline PCMs exhibit a relatively high resistivity which is the consequence of a Peierls distortion^{65,66} that is documented for GeTe and GST225,^{67–69} manifests by a departure of a perfect octahedral geometry with short and long bonds, and is linked with Fermi surface nesting in the nearly half-filled p-band.⁷⁰ The lattice distortion is, indeed, the result of the opening of pseudogap at the Fermi level which results from lowering the energy of the occupied electronic states. As a result, measured Drude low-frequency infrared conductivities,⁷¹ optical absorbance⁷² or calculated permittivities⁷³ are usually high, compared to the amorphous phase.

With the increased fraction of tetrahedra, in addition to the absence of long-range translational order, an increased bond localization sets in the amorphous phase (Figure 3A vs. Figure 6), and reduces the possibility of having electron–lattice interactions, albeit both T-Ge and R-Ge geometries display poorly localized states in the gap region which manifest by a decrease of the IPR close to E_F (Figure 6B,C). This means that electronic excitations in the amorphous phase can be achieved by various means, including Peierls distortion but these do apply on a minority of Ge sites. Recent measurements of dielectric properties of PCMs indicate²² that crystallization is accompanied by a huge increase in the Born effective charges, which suggests a significant change of bonding between the crystalline and the amorphous state. As a matter of fact, the representation of localization properties for c-GeTe, and contributions from R-Ge and T-Ge indicate that this is, indeed, the case for both s- and p-bands (Figure 6B,C).

5 | CONCLUSION

Taken together, these results show that the presence of distinct geometries between amorphous and crystalline phases can be rationalized from topological constraints and used for the analysis of their respective electronic and dielectric properties. The discussion on the presence of tetrahedral Ge is now unambiguously addressed and closes a debate that has been going on in the literature. In this respect, glassy PC tellurides appear to be somewhat unique. One of the main rules of Zachariasen's theory⁷ states, indeed, that similar building units should exist in both crystals and glasses as, for example, the $\text{SiO}_{4/2}$ tetrahedra present in both quartz or silica. Here, while c-PCMs display an obvious octahedral arrangement arising from a near rocksalt cubic structure,³⁷ SRO is obviously different in the amorphous phase with geometries that mimic either the first coordination shell of a typical tetrahedral glass (Figure 9A) or a complex bond arrangement made of short and long bonds in various geometries, partly octahedral and reminiscent of the crystalline phase.

ACKNOWLEDGMENTS

H.F.-R. gratefully acknowledges the computing time granted by LANCAD and CONACYT on the supercomputer Yoltla/Miztli/Xiuhcoatl at LSVP UAM-Iztapalapa/DGTIC UNAM/CGSTIC CINVESTAV. M.M. acknowledges access to the computer Roméo at Université de Reims-Champagne-Ardenne. This work is supported by the Mexico-France collaborative program CONACYT 321139/ECOS-Nord M21P01.

ORCID

M. Micoulaut  <https://orcid.org/0000-0002-0273-0563>

H. Flores-Ruiz  <https://orcid.org/0000-0001-7150-3957>

REFERENCES

- Sahoo D, Naik R. GSST phase-change materials and its utilization in optoelectronic devices: a review. *Mater Res Bull.* 2022;148:111679.
- Wuttig M, Bhaskaran H, Taubner T. Phase-change materials for non-volatile photonic applications. *Nat Photonics.* 2017;11:465–76.
- Zhang W, Ma E. Unveiling the structural origin to control resistance drift in phase-change memory materials. *Mater Today.* 2020;41:156–76.
- Boochood P, Micoulaut M. Topology of disordered networks and their applications. *Front Mater.* 2020;7:175.
- Micoulaut M, Flores-Ruiz H. Search for a possible flexible-to-rigid transition in models of phase-change materials. *Phys Rev B.* 2021;103:134206.
- Kolobov AV, Fons P, Tominaga J. Local instability of p-type bonding makes amorphous GeTe a lone-pair semiconductor. *Phys Rev B.* 2013;87:155204.
- Zachariasen W. The atomic structure in glass. *J Am Chem Soc.* 1932;54:3841–51.
- Prasai K, Biswas P, Drabold D. Electrons and phonons in amorphous semiconductors. *Semicond Sci Technol.* 2016;31:073002.
- Kolobov AV, Fons P, Frenkel AI, Ankudinov AL, Tominaga J, Uruga T. Understanding the phase-change mechanism of rewritable optical media. *Nat Mater.* 2004;3:703–8.
- Micoulaut M, Gunasekera K, Ravindren S, Boochood P. Quantitative measure of tetrahedral- sp^3 geometries in amorphous phase-change alloys. *Phys Rev B.* 2014;90:094207.
- Marchenko AV, Terukov E, Nasredinov F, Seregin PP. Local structure of amorphous and crystalline $\text{Ge}_2\text{Sb}_2\text{Te}_5$ films. *Tech Phys Lett.* 2020;46:958–60.
- Akola J, Jones RO. Structural phase transitions on the nanoscale: the crucial pattern in the phase-change materials $\text{Ge}_2\text{Sb}_2\text{Te}_5$ and GeTe. *Phys Rev B.* 2007;76:235201.
- Akola J, Jones R. Density functional study of amorphous, liquid and crystalline $\text{Ge}_2\text{Sb}_2\text{Te}_5$: homopolar bonds and/or AB alternation? *J Phys: Condens Matter.* 2008;20:465103.
- Kalikka J, Akola J, Larrucea J, Jones RO. Nucleus-driven crystallization of amorphous $\text{Ge}_2\text{Sb}_2\text{Te}_5$: a density functional study. *Phys Rev B.* 2012;86:144113.
- Raty JY, Zhang W, Luckas J, Chen C, Mazzarello R, Bichara C, Wuttig M. Aging mechanisms in amorphous phase-change materials. *Nat Commun.* 2015;16:7467.
- Raty J-Y. Aging in phase-change materials: getting insight from simulation. *Phys Status Solidi.* 2019;13:1800590.
- Hegedüs J, Elliott S. Microscopic origin of the fast crystallization ability of Ge–Sb–Te phase-change memory materials. *Nat Mater.* 2008;7:399–405.
- Hosokawa S, Pilgrim W-C, Höhle A, Szubrin D, Boudet N, Bézar J-F, Maruyama K. Key experimental information on intermediate-range atomic structures in amorphous $\text{Ge}_2\text{Sb}_2\text{Te}_5$ phase-change material. *Br J Appl Phys.* 2012;111:083517.
- Huang B, Robertson J. Bonding origin of optical contrast in phase-change memory materials. *Phys Rev B.* 2010;81:081204.

20. Shportko K, Kremers S, Woda M, Lencer D, Robertson J, Wuttig M. Resonant bonding in crystalline phase-change materials. *Nat Mater*. 2008;7:653–58.
21. Robertson J, Xiong K, Peacock P. Electronic and atomic structure of $\text{Ge}_2\text{Sb}_2\text{Te}_5$ phase-change memory material. *Thin Solid Films*. 2007;515:7538–41.
22. Chen C, Jost P, Volker H, Kaminski M, Wirtsohn M, Engelmann U, et al. Dielectric properties of amorphous phase-change materials. *Phys Rev B*. 2017;95:094111.
23. Grimme S. Density functional theory with London dispersion corrections. *Wiley Interdiscip Rev: Comput Mol Sci*. 2011;1:211–28.
24. Micoulaut M. Communication: Van der Waals corrections for an improved structural description of telluride-based materials. *J Chem Phys*. 2013;138:061103.
25. Micoulaut M, Piarristeguy A, Flores-Ruiz H, Pradel A. Towards accurate models for amorphous GeTe: crucial effect of dispersive van der Waals corrections on the structural properties involved in the phase-change mechanism. *Phys Rev B*. 2017;96:184204.
26. Kohara S, Kato K, Kimura S, Tanaka H, Usuki T, Suzuya K, et al. Structural basis for the fast phase change of $\text{Ge}_2\text{Sb}_2\text{Te}_5$: ring statistics analogy between the crystal and amorphous states. *Appl Phys Lett*. 2006;89:201910.
27. Perdew JP, Ruzsinszky A, Csonka GI, Vydrov OA, Scuseria GE, Constantin LA, et al. Restoring the density-gradient expansion for exchange in solids and surfaces. *Phys Rev Lett*. 2008;100:136406.
28. Micoulaut M, Coulet M-V, Piarristeguy A, Johnson MR, Cuello GJ, Bichara C, et al. Effect of concentration in Ge–Te liquids: a combined density functional and neutron scattering study. *Phys Rev B*. 2014;89:174205.
29. Micoulaut M, Flores-Ruiz H, Pradel A, Piarristeguy A. Piarristeguy, A. Tetrahedral complexity in amorphous networks: a possible clue for the unique properties of phase-change materials. *Phys Status Solidi*. 2021;15:2000490.
30. Ghezzi GE, Raty JY, Maitrejean S, Roule A, Elkaim E, Hippert F. Effect of carbon doping on the structure of amorphous GeTe phase-change material. *Appl Phys Lett*. 2011;99:151906.
31. Flores-Ruiz H, Micoulaut M, Coulet M-V, Piarristeguy AA, Johnson MR, Cuello GJ, Pradel A. Effect of tellurium concentration on the structural and vibrational properties of phase change Ge–Sb–Te liquids. *Phys Rev B*. 2015;92:134205.
32. Noé P, Sabbione C, Castellani N, Veux G, Navarro G, Sousa V, et al. Structural change with the resistance drift phenomenon in amorphous GeTe phase-change materials' thin films. *J Phys D: Appl Phys*. 2015;49:035305.
33. Stellhorn JR, Hosokawa S, Kaiser B, Kimura K, Boudet N, Blanc N, et al. The structure of the amorphous $(\text{GeTe})_{1-x}(\text{Sb}_2\text{Te}_3)_x$ System and implications for its phase-change properties. *Z Phys Chem*. 2021;235:141–67.
34. Piarristeguy A, Micoulaut M, Escalier R, Jóvári P, Kaban I, van Eijk J, et al. Structural singularities in $\text{Ge}_x\text{Te}_{100-x}$ films. *J Chem Phys*. 2015;143:074502.
35. Stellhorn JR, Hosokawa S, Pilgrim W-C, Blanc N, Boudet N, Tajiri H, Kohara S. Short-and intermediate-range order in amorphous GeTe. *Phys Status Solidi B*. 2016;253:1038–45.
36. Kononov A, Castro RA, Saito Y, Fons P, Bordovsky G, Anisimova N, Kolobov A. Dielectric relaxation in amorphous and crystalline Sb_2Te_3 thin films. *J Mater Sci*. 2021;32:14072–78.
37. Chatterji T, Kumar C, Wdowik UD. Anomalous temperature-induced volume contraction in GeTe. *Phys Rev B*. 2015;91:054110.
38. Shevchik N, Tejada J, Langer D, Cardona M. Valence bands of amorphous and crystalline GeTe determined by X-ray and UV photoemission. *Phys Status Solidi B*. 1973;57:245–56.
39. Kim J-J, Kobayashi K, Ikenaga E, Kobata M, Ueda S, Matsunaga T, et al. Electronic structure of amorphous and crystalline $(\text{GeTe})_{1-x}(\text{Sb}_2\text{Te}_3)_x$ investigated using hard X-ray photoemission spectroscopy. *Phys Rev B*. 2007;76:115124.
40. Micoulaut M, Piarristeguy A, Masson O, Escalier R, Flores-Ruiz H, Pradel A. Alteration of structural, electronic, and vibrational properties of amorphous GeTe by selenium substitution: an experimentally constrained density functional study. *Phys Rev B*. 2021;104:144204.
41. Raty J-Y, Otjacques C, Gaspard J-P, Bichara C. Amorphous structure and electronic properties of the $\text{Ge}_1\text{Sb}_2\text{Te}_4$ phase-change material. *Solid State Sci*. 2010;12:193–98.
42. Micoulaut M. Concepts and applications of rigidity in non-crystalline solids: a review on new developments and directions. *Adv Phys X*. 2016;1:147–75.
43. Yildirim C, Raty J-Y, Micoulaut M. Revealing the role of molecular rigidity on the fragility evolution of glass-forming liquids. *Nat Commun*. 2016;7:11086.
44. Chakraborty S, Boolchand P, Micoulaut M. Structural properties of Ge-S amorphous networks in relationship with rigidity transitions: an ab initio molecular dynamics study. *Phys Rev B*. 2017;96:094205.
45. Krbal M, Kolobov A, Fons P, Mitrofanov K, Tamenori Y, Hegedüs J, et al. Selective detection of tetrahedral units in amorphous GeTe-based phase-change alloys using Ge L3-edge X-ray absorption near-edge structure spectroscopy. *Appl Phys Lett*. 2013;102:209901.
46. Drabold D, Li Y, Cai B, Zhang M. Urbach tails of amorphous silicon. *Phys Rev B*. 2011;83:045201.
47. Pan Y, Inam F, Zhang M, Drabold D. Atomistic origin of Urbach tails in amorphous silicon. *Phys Rev Lett*. 2008;100:206403.
48. Boys, S. Quantum theory of atoms, molecules, and the solid state. Academic Press, New York; 1966. p. 253.
49. Marx, D, Hutter, J. Ab initio molecular dynamics: basic theory and advanced methods. Cambridge University Press; 2009.
50. Wannier GH. The structure of electronic excitation levels in insulating crystals. *Phys Rev*. 1937;52:191.
51. Marzari N, Vanderbilt D. Maximally localized generalized Wannier functions for composite energy bands. *Phys Rev B*. 1997;56:12847.
52. Silvestrelli PL, Marzari N, Vanderbilt D, Parrinello M. Maximally-localized Wannier functions for disordered systems: application to amorphous silicon. *Solid State Commun*. 1998;107:7–11.
53. Gageot M-P, Vuilleumier R, Sprik M, Borgis D. Infrared spectroscopy of *N*-methylacetamide revisited by ab initio molecular dynamics simulations. *J Chem Theory Comput*. 2005;1:772–89.
54. Rotenberg B, Salanne M, Simon C, Vuilleumier R. From localized orbitals to material properties: building classical force fields for nonmetallic condensed matter systems. *Phys Rev Lett*. 2010;104:138301.
55. Bauchy M, Micoulaut M, Celino M, Le Roux S, Boero M, Massobrio C. Angular rigidity in tetrahedral network glasses with changing composition. *Phys Rev B*. 2011;84:054201.

56. Resta, R, Vanderbilt, D. Theory of polarization: a modern approach. *Physics of ferroelectrics: a modern perspective*. Springer; 2007. p. 31–68.
57. Aguado A, Bernasconi L, Jahn S, Madden PA. Multipoles and interaction potentials in ionic materials from plane-wave-DFT calculations. *Faraday Discuss*. 2003;124:171–84.
58. Bernasconi L, Madden PA, Wilson M. Ionic to molecular transition in AlCl_3 : an examination of the electronic structure. *Phys Chem Commun*. 2002;5:1–11.
59. Molina JJ, Lectez S, Tazi S, Salanne M, Dufrêche J-F, Roques J, et al. Ions in solutions: determining their polarizabilities from first-principles. *J Chem Phys*. 2011;134:014511.
60. Baroni A, Pacaud F, Salanne M, Micoulaut M, Delaye J-M, Zeidler A, et al. Many-body effects at the origin of structural transitions in B_2O_3 . *J Chem Phys*. 2019;151:224508.
61. Silvestrelli PL, Martin E, Boero M, Bouzid A, Ori G, Massobrio C. Atomic structure of glassy GeTe_4 as a playground to assess the performances of density functional schemes accounting for dispersion forces. *J Phys Chem B*. 2020;124:11273–79.
62. Micoulaut M, Raty J-Y, Otjacques C, Bichara C. Understanding amorphous phase-change materials from the viewpoint of Maxwell rigidity. *Phys Rev B*. 2010;81:174206.
63. Bouzid A, Le Roux S, Ori G, Boero M, Massobrio C. Origin of structural analogies and differences between the atomic structures of GeSe_4 and GeS_4 glasses: a first principles study. *J Chem Phys*. 2015;143:034504.
64. Caravati S, Colleoni D, Mazzarello R, Kühne T, Krack M, Bernasconi M, Parrinello M. First-principles study of nitrogen doping in cubic and amorphous $\text{Ge}_2\text{Sb}_2\text{Te}_5$. *J Phys: Condens Matter*. 2011;23:265801.
65. Mott, N. *Metal-insulator transitions*. CRC Press; 2004.
66. Peierls, R, Peierls, RE. *Quantum theory of solids*. Oxford University Press; 1955.
67. Bichara C, Johnson M, Gaspard JP. Octahedral structure of liquid $\text{Ge}_2\text{Sb}_2\text{Te}_4$ alloy: first principles molecular dynamics study. *Phys Rev B*. 2007;75:060201.
68. Wuttig M, Lüsebrink D, Wamwangi D, Wełnic W, Gilleßen M, Dronskowski R. The role of vacancies and local distortions in the design of new phase-change materials. *Nat Mater*. 2007;6:122–28.
69. Raty J-Y, Wuttig M. The interplay between Peierls distortions and metavalent bonding in IV–VI compounds: comparing GeTe with related monochalcogenides. *J Phys D: Appl Phys*. 2020;53:234002.
70. Johannes M, Mazin I. Fermi surface nesting and the origin of charge density waves in metals. *Phys Rev B*. 2008;77:165135.
71. Shakhvorostov D, Nistor RA, Krusin-Elbaum L, Martyna GJ, Newns DM, Elmegreen BG, et al. Evidence for electronic gap-driven metal-semiconductor transition in phase-change materials. *Proc Natl Acad Sci*. 2009;106:10907–11.
72. Wełnic W, Wuttig M, Botti S, Reining L. Local atomic order and optical properties in amorphous and laser-crystallized GeTe . *C R Phys*. 2009;10:514–27.
73. Wełnic W, Botti S, Reining L, Wuttig M. Origin of the optical contrast in phase-change materials. *Phys Rev Lett*. 2007;98:236403.

How to cite this article: Micoulaut M, Flores-Ruiz H. Impact of structural short-range order and tetrahedral germanium on electronic and dielectric properties in phase-change materials. *J Am Ceram Soc*. 2024;107:2260–71. <https://doi.org/10.1111/jace.19608>